Journal of Materials Research and Technology 39 (2025) 8984–8993

Contents lists available at ScienceDirect

Journal of Materials Research and Technology

journal homepage: www.elsevier.com/locate/jmrt

Compositional requirements for the synthesis of Fe–Mn–C austenite-martensite composites: Beyond local equilibrium considerations in pearlite formation

Marcel Muench [a], Reza Gholizadeh [b], Myeong-heom Park [b], Nobuhiro Tsuji [b], Martin Peterlechner [c], Yolita M. Eggeler [c], Jan L. Riedel [a], Michael K. Eusterholz [a,d], Martin Heilmaier [a], Alexander Kauffmann [e,*]

[a] Institute for Applied Materials (IAM-WK), Karlsruhe Institute of Technology (KIT), Kaiserstraße 12, 76131, Karlsruhe, Germany
[b] Department of Materials Science and Engineering, Kyoto University, Sakyo-kyu, Kyoto, 606-8501, Japan
[c] Laboratory for Electron Microscopy (LEM), Karlsruhe Institute of Technology (KIT), Engesserstr. 7, 76131, Karlsruhe, Germany
[d] Karlsruhe Nano Micro Facility (KNMFi), Karlsruhe Institute of Technology (KIT), Hermann-von-Helmholtz-Platz 1, Eggenstein-Leopoldshafen, 76344, Germany
[e] Institute for Materials (IM), Ruhr University Bochum (RUB), Universitätsstraße 150, 44780, Bochum, Germany

ARTICLE INFO

Keywords:
Pearlite
Austenite
Martensite
Fe–Mn–C
Transformation

ABSTRACT

Recently, a new generation of high strength steels was introduced by utilizing a lateral chemical pattern of an austenite stabilizer to create microstructures of austenite γ and martensite α′ after quenching. A ternary Fe–Mn–C pearlite is a suitable initial state for this if Mn effectively partitions into the cementite. In the present study, two model Fe–Mn–C alloys were pearlite treated outside the well-established local equilibrium, Mn partitioning regime (P-LE). A complete pearlite formation was achieved not only for Fe-3.0Mn-3.0C (at.%, Alloy A) at high pearlite formation temperature but also for Fe-6.9Mn-3.2C (at.%, Alloy B) at low transformation temperature. The morphology of the pearlite included fine-scaled fibers and lamellae. Even though outside the P-LE region, significant Mn partitioning into cementite was obtained for both alloys. Pearlite was formed at approximately the overall Mn content, while growing either enriched or depleted in C for most of the reaction. The successful application of a short time austenitization treatment was proven for both alloys transforming the pearlite into α' + γ microstructures while retaining the initial pearlite morphology. Thus, fine-structured α' + γ can be synthesized from pearlite processed well outside the established Mn partitioning regimes, opening a much larger compositional and processing space.

1. Introduction

So-called *advanced high-strength steels* (AHSS) aim to achieve exceptional combinations of strength and ductility. Their properties arise from deliberate microstructural design that activates multiple, often concurrent, strengthening mechanisms, such as displacive phase transformations, deformation twinning, grain refinement, interfacial strengthening, and precipitation hardening [1–8]. Among the numerous alloying elements explored, Mn plays a particularly decisive role in some AHSS. By stabilizing austenite and influencing the stacking fault energy (SFE), Mn enables the formation of microstructures that are partially or entirely austenitic with tunable metastability. As highlighted by Raabe et al. [8], this tunability allows the activation of transformation-induced plasticity (TRIP) and twinning-induced plasticity (TWIP) mechanisms, which provide extraordinary strain-hardening capacity and damage tolerance for many AHSS. Depending on the overall composition and processing, such alloys may undergo diffusion-controlled and/or displacive phase transformations, element partitioning of interstitial and substitutional solutes, severe grain refinement, formation and/or dissolution of precipitates, etc. While these individual phenomena are well established, their integrated exploitation in a single, optimally balanced microstructure remains a key challenge in AHSS design [8].

In this context, Sun et al. [9] introduced a promising processing concept within the Fe–Mn–C system that addresses this challenge. Their routine consists of just two heat treatments: i) An initial pearlite formation treatment that creates a nanosized, lamellar Mn pattern, with

* Corresponding author.
E-mail address: alexander.kauffmann@rub.de (A. Kauffmann).

https://doi.org/10.1016/j.jmrt.2025.11.194
Received 5 October 2025; Received in revised form 12 November 2025; Accepted 23 November 2025
Available online 24 November 2025

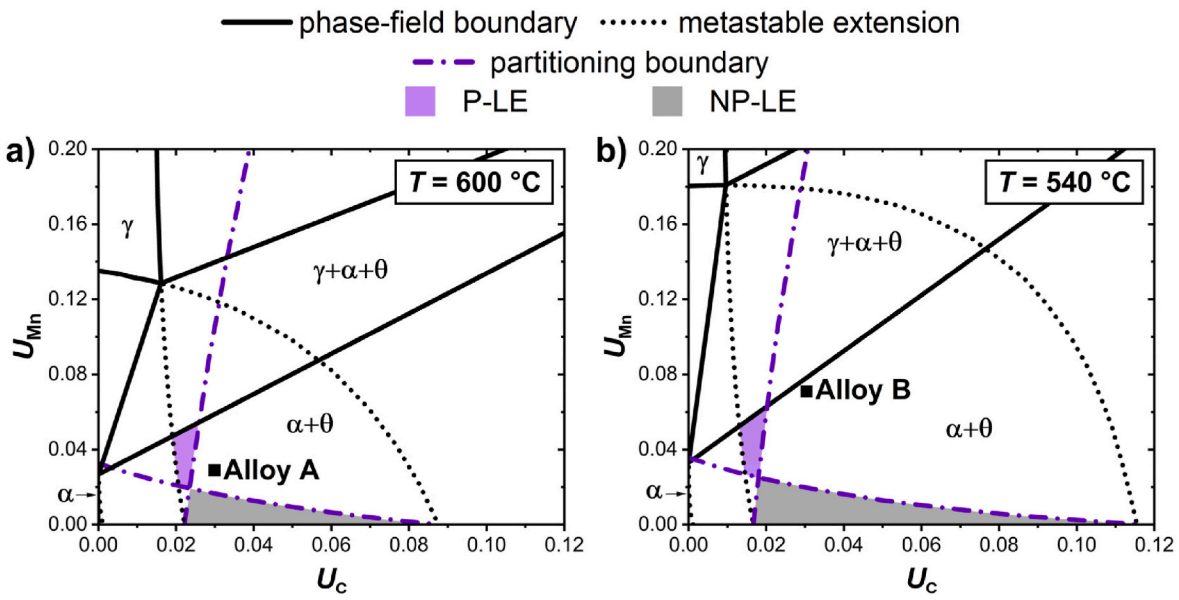

Fig. 1. Fe–Mn–C isothermal sections at a) 600 °C and b) 540 °C. BBlack bold lines illustrate the phase fields in GE. Black dotted lines indicate the metastable extrapolations of the α + γ and γ + θ phase field boundaries. The purple dot-dashed lines represent Mn partitioning boundaries for α (near horizontal) and θ (near vertical). P-LE and NP-LE regions are marked purple and gray, respectively. Alloys A and B, both lie outside these regions. The experimentally determined compositions listed in Tables 2 and 3 are displayed.

α-(Fe,Mn,C) ferrite being depleted and θ-$(Fe,Mn)_3C$ cementite being enriched in Mn. ii) A short time austenitization (STA) follows which leads to a complete transformation to γ-(Fe,Mn,C) while preserving the Mn pattern. Upon quenching of the inhomogeneous γ-(Fe,Mn,C), the Mn-depleted regions transform into α'-(Fe,Mn,C) martensite, while the Mn-enriched regions remain as metastable γ-(Fe,Mn,C), creating a novel ultrafine, lamellar microstructure. The application on a hypoeutectoid Fe-4.3Mn-2.3C (in at.%, Fe-4.4Mn-0.5C in wt.%) with additional tempering treatments leads to remarkable ultimate tensile strength and strain to failure combinations of 1.6–2.1 GPa and 7–10 % [9]. In addition to the promising mechanical capabilities of such microstructural conditions, the underlying processing provides the unique ability to purposefully manipulate microstructure parameters, i.e. lamellar spacing, colony size, phase fractions and phase stability. The relevant phases will be subsequently abbreviated as γ (austenite), α' (martensite), θ (cementite) and α (ferrite).

To test the limits of this scheme [9], one obvious possibility would be the variation of the alloy composition. The final microstructure and therefore also the resulting mechanical properties are expected to strongly depend on the initial Mn pattern. Therefore, changing the overall Mn content would be a feasible objective for tailoring both the microstructure and the mechanical response. Nonetheless, the recent endeavors on this topic [9–13], including the original work, strictly focus on Mn contents in a range of only 2–5 at.% Mn and a C content that results in an overall hypoeutectoid composition. This narrow compositional range might be rationalized by what was suggested in the early work of Hutchinson et al. [14] on the growth kinetics and local equilibrium (LE) conditions of Fe–Mn–C pearlite. To predict Mn partitioning during the eutectoid reaction, they developed two distinct LE design principles for transformations occurring in the three-phase region of α + θ + γ and another for the two-phase region of α + θ, that can be utilized simply via CALPHAD. The authors then restrict the application of these LE models to a temperature- and composition-dependent parameter space, the so-called *partitioning under local equilibrium* (P-LE) regime. The eutectoid reaction then likely commences under full LE conditions accompanied by partitioning of both Mn and C. For a given isothermal section, the compositional range that simultaneously falls within this regime and the α + θ two-phase region is very narrow [14]. This is consistent with the alloy compositions and temperatures investigated in Refs. [9–13].

It must be emphasized that the P-LE regime for pearlite formation itself is not an independent concept, but rather an outcome from a LE design approach originally developed for the pro-eutectoid α and θ reactions. This approach considers the vastly different diffusion coefficients of interstitial, fast-diffusing C compared to substitutional, slow-diffusing Mn [15–17], with diffusivity ratios in the order of 10^4–10^6 [17]. A direct result of the model are Mn partitioning boundaries that mark the compositional and temperature transition to a reaction where Mn partitioning is no longer thermodynamically necessary between α/γ and θ/γ. These boundaries then divide the two-phase-fields into two regimes: (i) A P-LE regime where partitioning of both Mn and C is expected during the reaction, and (ii) a negligible partitioning (NP-LE) regime, where partitioning can be restricted to only C whilst maintaining full LE at the reaction front. This condition is a special type of paraequilibrium and is also often referred to as quasi-paraequilibrium [15].

These fundamentals have first been transferred qualitatively from the pro-eutectoid reactions to pearlite formation by Coates and Hillert [15,17], as the corresponding reaction front exhibits LEs for both α/γ and θ/γ. With the simultaneous application of both partitioning boundaries, like for each pro-eutectoid reaction, two major regimes were derived: (i) again a P-LE regime, where the partitioning criteria with γ are fulfilled for *both* α and θ and (ii) a NP-LE regime where the criteria are *not* satisfied for either of the two. As the pearlite formation with a sufficiently strong Mn partitioning is a prerequisite for the aforementioned processing route, the introduction of these regimes heavily restricts the applicable range of alloy compositions and transformation temperatures, as staying inside the P-LE regime seemed reasonable, while NP-LE would be avoided [9–14].

What has not been experimentally addressed in literature thus far is the existence of an additional third and fourth regime besides P-LE and NP-LE. In these regimes, only one of the two partitioning criteria is fulfilled, either for α/γ or θ/γ. In case of a complete pearlite transformation, the partitioning of Mn between γ and one of the two product phases should already be sufficient to produce partitioning in the product phases. The regime of interest for this work is the one that fulfills the Mn partitioning criterion for α, but not for θ. It includes a large range of temperatures and compositions, especially at higher Mn and C contents, which have yet to be tested for Mn partitioning and the

possibility to apply the intended STA processing. However, with increasing Mn content the eutectoid line as well as the three-phase-field that separates the γ single-phase-field and the α + θ two-phase-field, shift to lower temperatures [18]. A lower transformation temperature as well as high contents of the slow-diffusing Mn will result in a currently unknown retardation of the pearlite transformation. Under such kinetically constrained conditions, the potential formation of metastable phases or alternative microstructures besides α + θ pearlite must also be considered. In Fe–Mn–C alloys, in particular, the possible precipitation of M_5C_2 [18] and $M_{23}C_6$ carbides, where M represents metallic elements, warrants attention, as their formation has been reported in Cr-rich and Al-rich Mn-containing steels [19,20].

Thus, the following research questions will be addressed in the present study.

R1: Does a pearlite treatment for a low Mn containing Fe-3.0Mn-3.0C (in at.%) at 600 °C and for a high Mn containing Fe-6.9Mn-3.2C (in at.%) at 540 °C result in an entirely transformed microstructure comprising pearlite that only consists of α and θ?
R2: Does pearlite in these Fe–Mn–C alloys exhibit considerable Mn partitioning into θ and how does it compare to global equilibrium (GE) and LE conditions?
R3: Is it possible to achieve a α' + γ microstructure by short-time austenitization from these pearlite conditions?

2. Simulations and experiments

2.1. Simulations

As mentioned in Sec. 1, out of the four regimes formed by the use of the two partitioning boundaries, only two have been addressed in literature thus far [14,15,17]: The P-LE regime and the NP-LE regime. For the pearlite transformation, these two regimes are uniquely defined by the fulfillment of the two independent Mn partitioning criteria between α/γ as well as θ/γ [14,15,17]. An extensive explanation on the construction of the resulting partitioning boundaries is presented in the Supplementary Material Fig. S1. Their application for a given isothermal section of the Fe–Mn–C system is shown in Fig. 1 as two dot-dashed purple lines. The representation in Fig. 1 is given by using the derived quantities:

$$U_C = X_C / (1 - X_C) \quad (1)$$

and

$$U_{Mn} = X_{Mn} / (1 - X_C) \quad (2)$$

according to the treatment by Hillert [15] as well as Coates [17] and Hutchinson [14]. A detailed explanation of the physical meaning and practical usage of these variables can be found in the Supplementary Material of this article. The thermodynamic data was obtained using the 2023 PanHEA database in the Pandat software provided by CompuTherm (USA). The theoretical data on the phase-field positions of the Fe–Mn–C system are in good agreement with experimental literature data in the relevant compositional range [9,18,21–29]. All additional thermodynamic LE considerations that are not captured by Pandat were obtained using self-developed Matlab scripts which are published public domain [30].

While both the regime to the left as well as to the right of the intersection of the two dot-dashed lines in Fig. 1 a) and b) remain unexplored, the regime on the right is the scope of the present article. It includes high overall Mn contents which hold the potential of stabilizing large fractions of γ in the final microstructure after STA. Here, the partitioning criteria are fulfilled for α, but not for θ formation. Inside this regime two model alloys, Alloys A and B, were selected. They lie inside the α + θ two-phase-field as well as inside the metastable extensions of the α + γ and γ + θ phase-field boundaries to avoid pro-eutectoid α or θ formation. The nominal composition is Fe-3.0Mn-3.0C (in at.%) for the Mn-lean Alloy A and Fe-6.9Mn-3.2C (in at.%) for the Mn-rich Alloy B. This corresponds to Fe-3.0Mn-0.7C and Fe-7.0Mn-0.7C in wt.% for Alloys A and B, respectively.

Table 1
Lattice constants of α and θ for Alloys A and B determined via synchrotron XRD.

	Phase	Lattice Constants		
		a	*b*	*c*
		Å		
Alloy A	α	2.868	–	–
	θ	5.080	6.748	4.520
Alloy B	α	2.868	–	–
	θ	5.091	6.755	4.529

2.2. Experiments

Alloy manufacturing was done by arc melting high purity bulk elements as well as an in-house synthesized Fe_3C obtained by the same method. The elements Mn (etched, nominal purity 99.8 %) and graphite (nominal purity 99.999 %) were provided by chemPUR GmbH (Germany). Fe (nominal purity 99.99 %) was provided by Alfa Aesar (United States). Arc melting was conducted in an AM/0.5 furnace provided by Edmund Bühler GmbH (Germany). The furnace chamber was evacuated to $5{\cdot}10^{-2}$ mbar and filled with Ar. This process was repeated for three times in total in order to purify the melting atmosphere. Then, a vacuum of less than $1{\cdot}10^{-4}$ mbar was established. The processing chamber was then filled with Ar once more to a pressure of 600 mbar. Residual O_2 within the furnace chamber was gettered by liquefying a Zr granule before melting the bulk elements. Every manufactured ingot was flipped and re-melted at least five times. The alloy ingots were homogenized utilizing a STF15/450 21–601449 tube furnace by Carbolite Gero GmbH & Co. KG (Germany) with flowing high purity Ar atmosphere. The heat treatment temperature was 1100 °C for a dwell time of 96 h. Heating and cooling were conducted at a rate of 115 K/h. The chemical composition was determined through optical emission spectroscopy (OES) by analyzing both, the top and bottom side after the last re-melting step. The results are displayed in Tables 2 and 3 for Alloys A and B, respectively. The standard deviation for all elements was determined to be < 0.07 at.% (0.07 wt%). Samples for further investigations were cut from the alloy batches using a high-speed rotatory cutting device (Struers, France).

Pearlite formation was carried out in air at atmospheric pressure using two pre-heated box furnaces. After completion of the prior austenitization step at 910 °C for 1 h, an immediate furnace transfer was performed. Pearlite in Alloys A and B was formed at 600 °C for 16 h and 540 °C for 96 h, respectively, based on initial trials to obtain relevant temperature/time combinations. The heat treatments were concluded by oil quenching.

The STA treatments were done in a pre-heated box furnace at 770 °C for 150 s and also concluded by oil quenching. To ensure a high heating rate, the samples were covered by pre-heated Al_2O_3 powder at the start of the treatment.

The samples for microstructure characterization were prepared by water-cooled grinding with SiC paper followed by standard metallographic polishing steps with 3 and 1 μm polycrystalline diamond suspensions. As a finishing step, polishing with MasterMet-2 by Buehler (USA) was performed for 5 min. Samples were subsequently etched in a 1 % Nital solution for 5 s. The grinding process was carried out to remove any decarburized layer that has formed during the heat treatments. Microstructure characterization was performed by scanning electron microscopy (SEM). For secondary electron (SEM-SE) as well as backscattered electron (SEM-BSE) contrast imaging, a Leo Gemini 1530 field-emission SEM by Zeiss (Germany) was utilized. Low magnification,

Table 2
Compositions X, C activity in γ a_C^γ, molar phase fractions f_m and U of Alloy A according to thermodynamic calculations (GE, SCA-LE), experimental (exp.) results from APT analyses and reconstructions. + denotes experimental data. # denotes experimental data adjusted according to the thermodynamic dataset. The other data was derived from the thermodynamic dataset.

Condition	Phase	Position	X_C	X_{Mn}	U_C	U_{Mn}	a_C^γ	f_m
Alloy A	–	–	0.029 +	0.028 +	0.030	0.029	–	–
GE	α	–	$1 \cdot 10^{-4}$	0.011	$1 \cdot 10^{-4}$	0.011	–	0.88
	θ	–	0.250	0.163	0.333	0.217	–	0.12
SCA-LE	α	γ	$1 \cdot 10^{-4}$	0.021	$1 \cdot 10^{-4}$	0.021	–	0.88
	θ	γ	0.250	0.080	0.333	0.106	–	0.12
	γ	α	0.031	0.114	0.032	0.118	0.29	–
		θ	0.020	0.027	0.020	0.027	0.29	–
Exp.	α	–	$1 \cdot 10^{-4}$ +	0.020 +	$1 \cdot 10^{-4}$	0.020	–	0.95 +
	θ	–	0.262 +	0.218 +	0.355	0.295	–	0.05 +
Reconstr.	α	γ	$1 \cdot 10^{-4\#}$	0.020#	$1 \cdot 10^{-4}$	0.020	–	0.95 +
	θ	γ	0.250#	0.222#	0.333	0.296	–	0.05 +
	γ	α	0.034	0.111	0.035	0.115	0.33	–
		θ	0.017	0.089	0.017	0.091	0.16	–

Table 3
Compositions X, C activity in γ a_C^γ, molar phase fractions f_m and U of Alloy B according to thermodynamic calculations (GE, SCA-LE), experimental (exp.) results from APT analyses and reconstructions. + denotes experimental data. # denotes experimental data adjusted according to the thermodynamic dataset. The other data was derived from the thermodynamic dataset.

Condition	Phase	Position	X_C	X_{Mn}	U_C	U_{Mn}	a_C^γ	f_m
Alloy B		–	0.029 +	0.069 +	0.030	0.071	–	–
GE	α	–	$1 \cdot 10^{-5}$	0.029	$1 \cdot 10^{-5}$	0.029	–	0.88
	θ	–	0.250	0.375	0.333	0.500	–	0.12
SCA-LE	α	γ	$1 \cdot 10^{-5}$	0.032	$1 \cdot 10^{-5}$	0.032	–	0.88
	θ	γ	0.250	0.350	0.333	0.466	–	0.12
	γ	α	0.013	0.179	0.013	0.181	0.09	–
		θ	0.010	0.147	0.010	0.148	0.09	
Exp.	α	–	$2 \cdot 10^{-4}$ +	0.020 +	$2 \cdot 10^{-4}$	0.020	–	0.80+
	θ	–	0.221 +	0.293 +	0.284	0.376	–	0.20 +
Reconstr.	α	γ	$1 \cdot 10^{-4\#}$	0.020#	$1 \cdot 10^{-4}$	0.020	–	0.80 +
	θ	γ	0.250#	0.282#	0.333	0.376	–	0.20 +
	γ	α	0.054	0.158	0.058	0.167	0.76	–
		θ	0.011	0.106	0.011	0.107	0.14	–

wide field of view micrographs with high resolution were obtained by automated stitching in Microsoft Image Composite Editor. The quantification of microstructural details including the area fractions of the constituting phases and morphologies was carried out using the ImageJ software. Estimates for the fractions of regions of similar morphology were done by manually selecting and asserting regions with θ aspect ratios close to one as fibrous. Fibers oriented parallel to the sample surface were therefore identified as lamellae. Micrographs for all analysis were selected randomly and at different magnification to enable both a large overall area of investigation as well as high accuracy of the imaging. The difference in total area mapped between different magnification micrographs was considered. The determined area fractions were converted into volume fractions under the assumption of isometry and isotropy. A more detailed assessment of parameters like θ spacing or θ morphology fraction would require 3D methods for microstructure analysis, e.g. FIB tomography, and was not scope of the present study.

Phase identification and determination of lattice constants was done by means of transmission synchrotron X-ray diffraction (XRD) at beamline BL13XU, SPring-8 of the Japan Synchrotron Radiation Research Institute (JASRI). The diffraction experiments were performed using monochromatic synchrotron radiation at an energy of 30 keV (λ = 0.0413 nm) and 30 s exposure time. The calibration of the 2θ zero-shift and sample displacement was done with a standard specimen of ceria

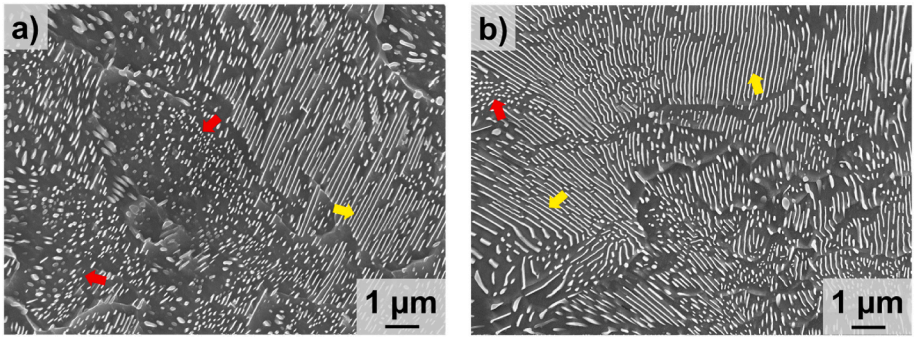

Fig. 2. SEM−SE micrographs (Nital etching) after completion of pearlite formation: a) Alloy A, 600 °C/16 h and b) Alloy B, 540 °C/96 h. No untransformed regions were found. θ appears light, α appears dark. Lamellar morphology is indicated by yellow, fibrous by red arrows. High resolution, wide field of view micrographs obtained from stitching are available via Ref. [33].

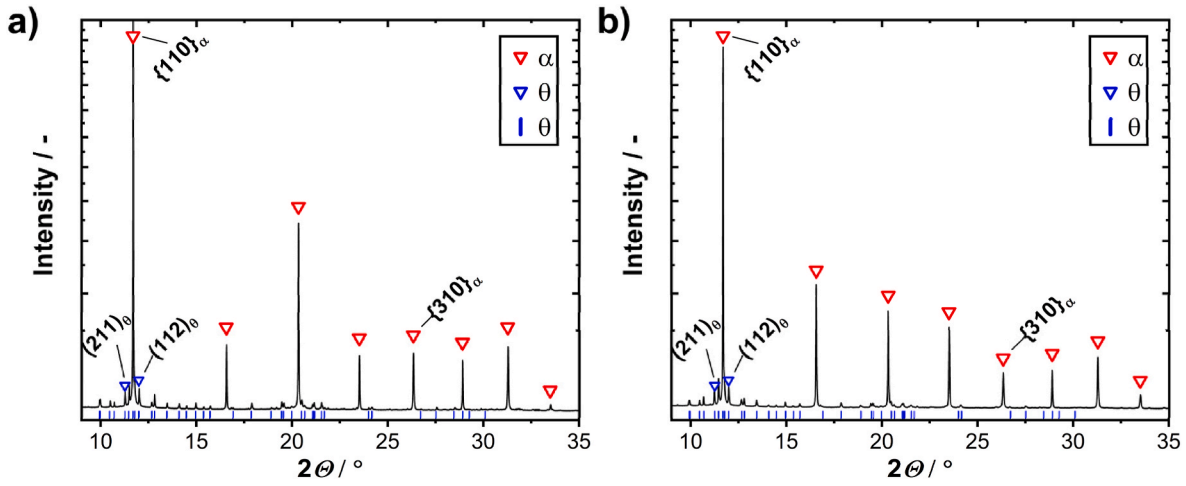

Fig. 3. Transmission XRD patterns of: a) Alloy A and b) Alloy B. The intensity is plotted as a function of 2Θ. Characteristic diffraction peaks corresponding to α are marked in red, while peaks associated with θ are highlighted in blue. All relevant peaks of θ are highlighted below the pattern, while the $(211)_\theta$ and $(112)_\theta$ peaks were used to uniquely identify the carbide. Note that due to the orthorhombic unit cell of θ individual sets of planes are indexed, while for cubic α the respective families of planes are indexed. The difference is highlighted by utilizing different parentheses.

(CeO_2). Additionally, local analysis of the constituting phases was performed via selected area electron diffraction (TEM-SAED) with a JEM-2100F by Jeol (Japan) and a Titan3 by FEI (USA) transmission electron microscope (TEM) operated at 200 kV and 300 kV, respectively. For determining the local composition of the phases, both energy dispersive X-ray spectroscopy in scanning TEM (STEM-EDS) as well as atom probe tomography (APT) were considered. However, due to significant inaccuracies introduced by quantifying the C content, APT was selected as the superior method both in terms of data accuracy and spatial resolution [31]. The experiments were performed on both alloys after pearlite formation with a LEAP 4000X HR by Cameca (France). Data presented in the main article were generated in voltage mode, while additional data depicted in the Supplementary Material were generated in laser mode. Tip preparation was done via focused ion beam (FIB) milling with an Auriga 60 by Zeiss (Germany). Tips presented in the Supplementary Material were coated with Cr to increase tip stability, following the routine used in Ref. [32]. Peak decomposition was required for the θ regions, which was applied by the integrated feature of the AP Suite 6.3 software (Cameca, France). The software decomposes overlapping peaks by considering the remaining unique peak(s) of the species of interest of the same charge and applies the relative natural abundances to weigh the contribution of that species to the initial peak. An example for this would be C_2^{1+} and C_4^{2+} in θ. Both species exhibit peaks at 24 and 25 Da. However, C_4^{2+} possesses a unique peak at 24.5 Da as well. Considering the natural abundances of the different C_4^{2+} isotopes, the contribution to the peak at 24 Da and 25 Da can be derived, which leaves the remaining counts of the peaks for C_2^{1+}.

3. Results and discussion

3.1. Pearlite formation

In Fig. 2, micrographs of both alloys are shown after their respective pearlite treatments: 600 °C/16 h for Alloy A and 540 °C/96 h for Alloy B. A complete transformation was achieved for both alloys. High resolution, wide-field-of-view micrographs achieved by stitching proving the statement are provided via a public repository [33].

With respect to pearlite morphology, a notable difference between the two alloys is obtained. Both exhibit extended regions of fibrous morphology, comprising volume fractions of (0.91 ± 0.08) and (0.32 ± 0.12) of the pearlite in Alloys A and B, respectively. The volume-specific phase fraction of θ is (0.06 ± 0.01) for Alloy A and (0.21 ± 0.02) for

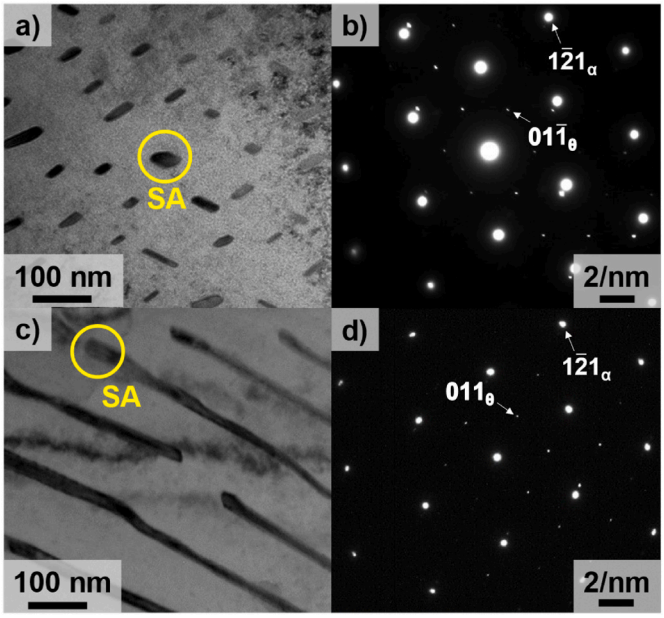

Fig. 4. TEM bright field micrographs (a),c)) and corresponding TEM-SAED patterns (b), d)) of: a), b) fibrous regions from Alloy A and c),d) lamellar region from Alloy B. The zone axes (ZA) in both b) and d) are $[111]_\alpha \parallel [100]_\theta$.

Alloy B. Alloy B frequently exhibits regions of increasing interface spacing towards the colony boundaries, thus, at potentially late stages of the transformation before completion. Due to their low overall fraction of (0.02 ± 0.01), these regions were not included in the randomly selected micrographs to determine the volume-specific phase fractions.

To identify the constituting phases of both alloys after the pearlite treatment, transmission XRD experiments were performed. Additionally, the corresponding lattice parameters were determined. Due to large pearlite colony size, preferred orientation and intensities different from powder diffraction patterns were obtained. This obstructs quantification of phase fractions. All analyzed peaks were exclusively attributed to either α or θ, as shown in Fig. 3 and no evidence for any other carbide than θ or untransformed γ was found. The $(211)_\theta$ and $(112)_\theta$ peaks were considered to uniquely identify the carbide as θ. The lattice constants of both phases are summarized in Table 1. The results indicate a similar

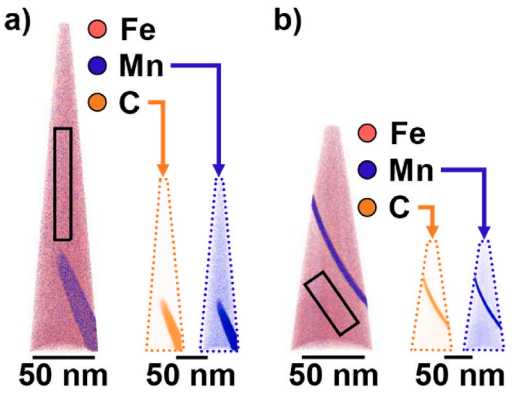

Fig. 5. Reconstructed APT tip of: a) Alloy A with a θ fiber and b) Alloy B with a θ lamella. Fe is represented in red, Mn in blue and C in orange. The fiber and lamella are enriched in C and Mn. For α, the volume that was used to determine the chemical composition is illustrated via the black boxes. For θ, the analyzed volume was selected inside a Mn iso surface to avoid the effect of interface regions.

chemical composition of α while a significant difference can be expected for θ.

Further characterization of the pearlite was done via TEM imaging and electron diffraction. Due to the large pearlite colony size, TEM specimens were taken from representative regions, i.e. a fibrous colony for Alloy A and a lamellar colony for Alloy B. Both lift outs were taken in regions of near constant interface spacing (73 ± 26 nm) and (104 ± 19 nm), respectively. Bright field micrographs as well as the TEM-SAED patterns are shown in Fig. 4. The zone axes in both Fig. 4 a) and d) are parallel to the $[100]_\theta$ direction following the lattice parameter convention, $b > a > c$ for θ. The lift outs were chosen perpendicular to the long fiber axes for Alloy A (Fig. 4 a)) and the lamellar plane for Alloy B (Fig. 4 c)). In such a scenario, fibrous and lamellar colonies of interest cannot be distinguished from one another as both appear similar at the sample surface. They can only be distinguished after cutting a FIB trench and subsequent cross-sectional imaging. For both samples, the transmission XRD results regarding the constituting α and θ phases were confirmed by TEM-SAED patterns in Fig. 4 b) and d), respectively. Furthermore, the orientation relationship (OR) was determined. The investigated colonies of Alloys A and B both exhibit variants of the Isaichev OR with $\langle 111\rangle_\alpha \parallel \langle 100\rangle_\theta$ and $\{1\bar{2}1\}_\alpha \parallel \{011\}_\theta$, which is well established for pearlite [34]. Please note that Fig. 4 a) for Alloy A exhibits a twin site of the OR with a $(01\bar{1})_\theta$ habit plane instead of $(011)_\theta$ as for Fig. 4 b). The θ twin variant is of compound character with the habit plane $(011)_\theta$, shear direction $[01\bar{1}]_\theta$ and shear plane $(100)_\theta$. Furthermore, the twin orientation can be achieved via a rotation of the θ matrix crystal around the $[100]_\theta$ direction by 111.8°. This equates to the angle between $(011)_\theta$ and $(01\bar{1})_\theta$ in the θ unit cell.

The Isaichev OR might mistakenly be expressed by defining the habit plane according to $\{0\bar{1}1\}_\alpha \parallel \{031\}_\theta$. This can be attributed to the very small angular mismatch (0.3°) between the sets of lattice planes involved. However, the angular mismatch becomes more apparent for high indexed spots.

Samples for APT were selected in similar fashion like the TEM specimens, i.e., lift out via FIB in a fibrous colony for Alloy A and in a lamellar colony for Alloy B, both within regions of nearly constant interface spacing. In total, four tips were analyzed with two for Alloy A stemming from the same colony and two for Alloy B from different colonies. One of each alloy is discussed as an example. The remaining data agrees with the statements and discussion. The data is included in Fig. S2, Fig. S3 and Table S1 of the Supplementary Material. To allow for a more detailed assessment of the chemical composition, the local phase fractions were determined at the lift out position from SEM−SE micrographs. The local θ volume fraction of Alloy A is 0.05, while it is 0.19 for Alloy B. These values were then converted to the local molar phase fractions f_m which are provided together with the values for α in Tables 2 and 3 for Alloys A and B, respectively.

Two reconstructed tips are depicted in Fig. 5. Both show Mn and C enrichment coinciding in the same region, a θ fiber (Fig. 5a)) for Alloy A and lamella (Fig. 5b)) for Alloy B. The determined C content of θ in all tips (Table 2, Table 3 and Table S1 in the Supplementary Material) deviates from the stoichiometric expectation, which may be explained by different phenomena. Possible scenarios are discussed in Ref. [35,36]. An additional aspect that could have affected the evaporation and, therefore, quantification of C is the difference in θ morphology. However, as the focus of this work is the Mn partitioning, this matter is not discussed further here.

While Alloy A shows a Mn content of 21.8 at.% (vs. 2.8 at.% in the alloy) within θ, Alloy B exhibits 29.3 at.% of Mn (vs. 6.9 at.% in the alloy). Thus, Mn partitioning takes place during the pearlite reaction for both alloys, regardless of being located outside the P-LE region in the isothermal sections of Fig. 1. A more detailed overview of the local chemical compositions, including the C contents, are shown in Tables 2 and 3 for Alloys A and B, respectively. The interface between α and θ was investigated for potential element segregation. Considering the spatial resolution limit of roughly 2 nm [31], all tips indicate practically sharp interfaces with no detectable segregation. The concentration profiles that were used for the analysis are shown in the Supplementary Material, Fig. S3 a,c) for the tips discussed in the main article and b), d) for the additional ones.

3.2. *Local equilibrium models and reaction kinetics*

The results presented in Sec. 3.1 show that pearlite formation can lead to significant Mn partitioning even when formed outside the P-LE regime. The P-LE and NP-LE regimes result directly from the Mn partitioning boundary lines for pro-eutectoid α and θ formation, see Fig. 1. These boundary lines originate from the LE design of the two reactions and describe the thermodynamic requirements of partitioning between α/γ and θ/γ, respectively. Taking pro-eutectoid α formation as an example: For each composition on the α partitioning boundary line, the LE predicts the same U_{Mn} within the forming α and the bulk γ. The forming α can thus dissolve the overall Mn content within the alloy, making Mn partitioning thermodynamically unnecessary. This condition is met for all compositions below this partitioning boundary for a given isothermal section (NP-LE for α formation). In case of pro-eutectoid θ formation, the same holds true for all compositions to the right of the boundary (NP-LE for θ formation). Hence, composition and temperature should be selected to lie in the respective P-LE regime if Mn partitioning is to be guaranteed during the reaction. For pearlite formation, where both partitioning boundaries are applied simultaneously, a similar argument is possible. This can be attributed to the fact that during the transformation, the forming α and θ are in contact with γ at the reaction front and are therefore expected to form two independent LEs between α/γ and θ/γ, respectively. For a complete pearlite transformation ($\gamma \rightarrow \alpha + \theta$ in the two-phase-field), elemental partitioning associated with the LE at the reaction front must be accommodated entirely by the product phases α and θ. Hence, it is reasonable to assume that already fulfilling a single partitioning criterion for pearlite formation inside the two-phase-field is sufficient to eventually achieve Mn partitioning between α and θ. In the present study, this is shown for the interesting region where the Mn partitioning criterion is fulfilled only for α. Consequently, possibilities of similar partitioning in the other regimes remain, i.e. the partitioning criterion is fulfilled for θ/γ but not for α/γ as well as the NP-LE regime with none of the two fulfilled. Following the prior argument, partitioning of Mn at either of the two interfaces must result in partitioned pearlite, if a complete transformation occurs and the overall Mn content exceeds its solubility in α. Within the NP-LE regime however, Mn partitioning between the two interfaces should be negligible and therefore finally also between α and

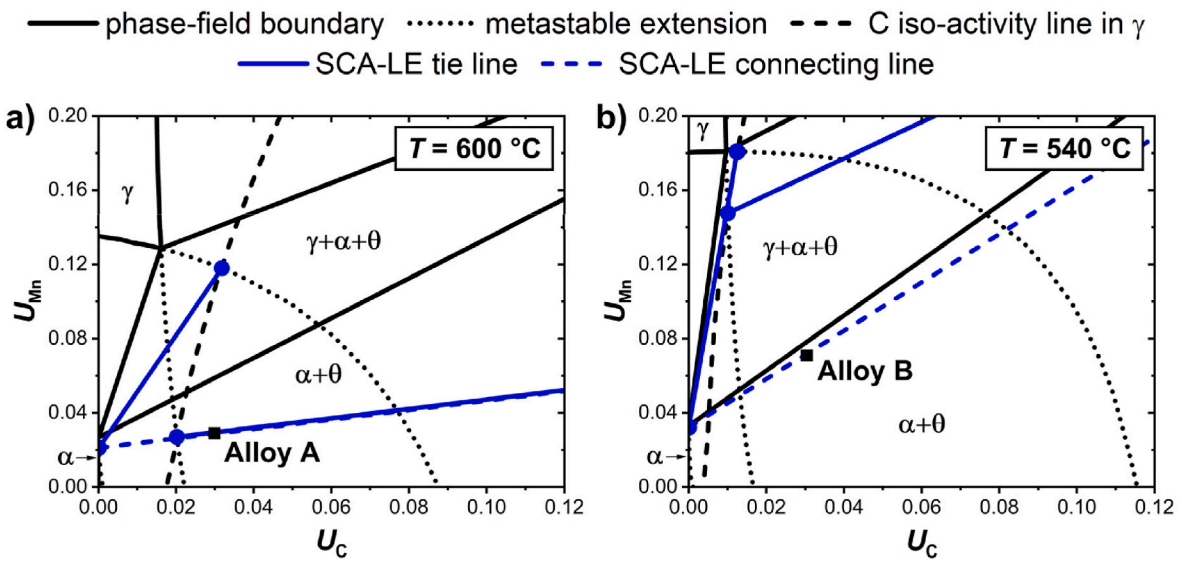

Fig. 6. Schematic design according to SCA-LE in isothermal sections: a) Alloy A at 600 °C and b) Alloy B at 540 °C. The illustration of the isothermal section is the same as for Fig. 1. The blue solid lines indicate tie lines while the blue dashed line is the line connecting θ and α forming during steady-state pearlite growth. The predicted enrichment of Mn in θ is: a) 8.0 at.% (vs. 2.8 at.% in Alloy A) and b) 35.0 at.% (vs. 6.9 at.% in Alloy B).

θ. Modelling such a transformation demands extremely sharp concentration profiles. Bhadeshia [37] argues, that these profiles are physically questionable. Based on the theory of spinodal decomposition [38–41], he derived substantial energetic penalties for such strong concentration gradients, so much that they are unlikely to occur. Supporting this theoretical derivation is the lack of experimental evidence of these sharp concentration spikes at the interface, which are summarized in Ref. [42]. This raises doubts on the transition between the LE conditions and even whether NP-LE exists for reconstructive phase transformations [37].

While the concept of the partitioning regimes, especially with respect to the existence of NP-LE is questionable, the LE model by Hutchinson et al. [14] for pearlite formed within the α + θ two-phase-field remains promising when it comes to predicting its composition. As it was designed independent of the pro-eutectoid reactions, its application is not restricted to the partitioning regimes, as shown in Fig. 6 a) and b) for Alloys A and B, respectively. The design principle is based on what was first proposed by Hillert (the original Ref. is summarized and reproduced in Ref. [43]) and later independently by Kirkaldy [16] that for simultaneous Mn and C partitioning, the driving force for C diffusion in γ ahead of the reaction front must be reduced to compensate for the orders of magnitude difference in diffusion coefficients of the elements. To achieve this condition for pearlite, Hutchinson et al. [14] demand that γ in contact with either growing θ or α are required to share the same C activity a_C^{γ}. The γ compositions ahead of θ and α are located on the same C iso-activity line in Fig. 6 (blue dots on the C iso-activity line at the intersections with the dotted, metastable extensions). The forming θ and α are obtained from following the tie lines (blue, solid lines) connected to these γ compositions. As Hutchinson et al. [14] experimentally obtained a steady-state growth of pearlite within the α + θ, two-phase-field

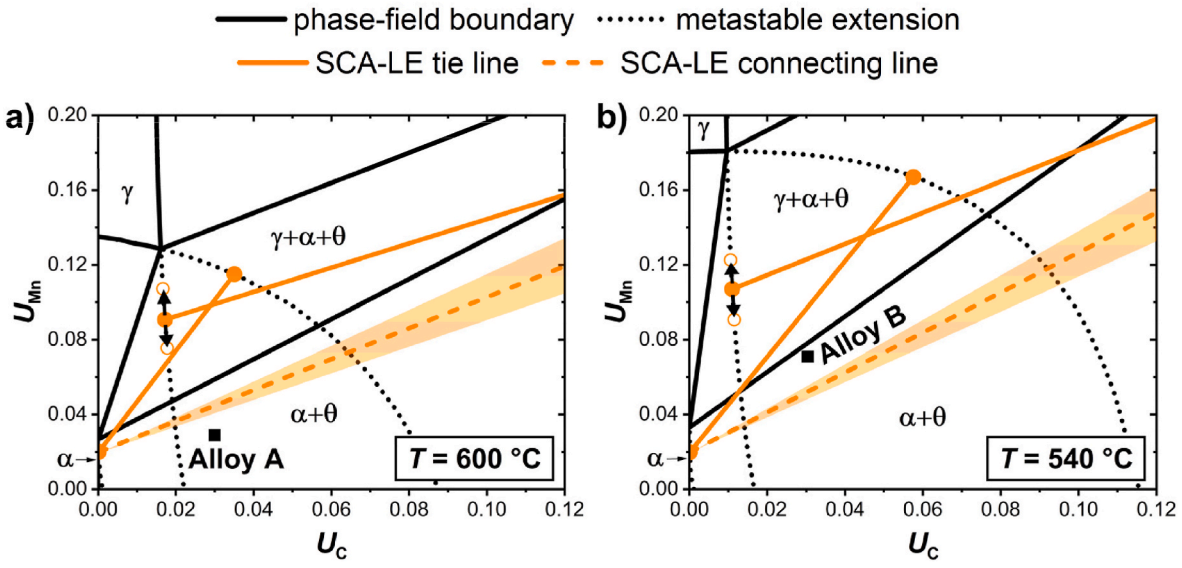

Fig. 7. Fe–Mn–C isotherms at: a) 600 °C and b) 540 °C. The illustration of the isothermal section is the same as for Fig. 1. The active tie lines (orange, full) as well as the line connecting (orange, dashed) the α and θ compositions are shown. The applied uncertainty for the composition of θ impacts both the position of the connecting line as well as the γ/θ tie line. The possible positions of the connecting line are indicated by an orange box. For the endpoints of the γ/θ tie line, the possible range is indicated by black arrows and open data points (orange). Alloys A and B both lie considerably off the connecting line.

with constant growth rate and interface spacing, an additional boundary condition regarding the overall composition of the growing pearlite was introduced. Namely, its composition must be consistent with the alloy composition. This can only be achieved when the connecting line (blue, dashed line) between the growing θ and α intersects the alloy composition. This connecting line does not represent a tie line as the two growing phases are not in equilibrium with each other. In what follows, this design principle is referred to as steady-state, C activity-based local equilibrium condition (SCA-LE). As depicted in Fig. 6, the application of the SCA-LE design indicates an enrichment of Mn in θ during pearlite formation even though it is being applied to Alloys A and B outside the P-LE regime.

They experimentally validated predicted pearlite compositions via STEM-EDS [14]. In the present work, APT was chosen as it allows an increased quantification accuracy for both C and Mn [31]. To re-evaluate the viability of the SCA-LE method, its main design principles are compared to the experimental data of Alloys A and B in the following. It is assumed that the experimentally determined compositions of α and θ (Tables 2 and 3 for Alloys A and B, respectively) correspond to their compositions during the reaction right after the reaction front has passed the region of interest. This assumption is based on the findings of Hutchinson et al. [14]. They determined the Mn content in partitioned Fe–Mn–C pearlite as a function of distance from the reaction front for a given transformation condition. In addition, pearlite colonies were analyzed at different stages of the transformation, i.e. after different hold times at the respective pearlite formation temperature. Both analyses suggest that when pearlite formation is performed in the two phase-field, the chemical composition of a specific region within a sample remains near constant even after extended hold times [14]. Since the pearlite treatment was terminated shortly after the complete transformation, a comparison between the SCA-LE model and post-transformation experimental LE data is viable. The APT data of the two product phases allows for a reconstruction of the γ/α and γ/θ tie lines, as each composition of the product phases may only be described by a single tie line. The validation will focus on whether the reconstructed tie line end points for the γ/α and γ/θ interfaces share the same C iso-activity and whether the connecting line between the α and θ compositions intersects the overall alloy composition.

For the γ/θ tie line reconstruction, the C content within the θ was set to 25.0 at.%. This was done via a count correction of the C ions and therefore the total amount of ions that were included in the APT analysis of θ. The resulting Mn content was then deliberately equipped with a conservative uncertainty of ±3.0 at.% to account for any inaccuracy introduced by the quantification of C. The α composition was not changed, however, as the determined composition does not lie exactly on the respective metastable phase-field extension, the reconstructed γ/α tie line slightly differs in its α composition. Fig. 7 shows the reconstructed tie lines as well as the connecting line for Alloys A and B in Fig. 7 a) and b), respectively. The compositions of all phases at the respective interfaces, as well as the C activities in γ a_C^γ are appended to Tables 2 and 3 as the reconstructed data. To further assist with the analysis, the GE condition that might be achieved after an infinitely long hold time is also given in Tables 2 and 3 for both alloys.

Considering Tables 2 and 3, the γ in contact with α and θ do not share the same C activity for the two alloys. This remains true even when a conservative uncertainty of the θ composition is considered.

Furthermore, the connecting line between α and θ does not intersect the alloy composition for both alloys. Such a scenario is only possible if the composition of the forming pearlite does not correspond to the overall composition of the alloy, i.e., the reaction does not meet steady-state conditions. Hutchinson et al. [14] already noted this and included such a possibility when introducing the SCA-LE model. As the C iso-activity line, which determines the local equilibria at the reaction front in SCA-LE, is not required to intersect the alloy composition, C diffusion between γ at the interface and the bulk is possible (when a difference in C activity exists). Despite this, the transformation follows apparent steady-state conditions for most of the duration, with a near constant interface velocity and interface spacing [14]. This growth continues until the change in C content within the diminishing γ becomes so drastic that an abrupt change in growth is required. In Fe–Mn–C pearlite, this may be expressed by a sudden increase or decrease in the interface spacing of the θ [14]. One aspect that must be mentioned in this context is that spacing alone is insufficient to describe this phenomenon. As C solubility in α and θ is either extremely small or at a stoichiometric 25 at.%, a drastic change in C content in the γ near the reaction front can only be accommodated by a shift in the product phase fractions. Additionally, an increase or decrease in interface spacing may be observed.

For the two cases depicted in Fig. 2, SCA-LE predicts that the activities in bulk γ are higher than in the near-interface γ. Thus, a diffusion flux of C towards the interface would be possible during most of the growth for both alloys, potentially depleting the bulk γ in C. In contrast, the reconstructions of the experimental results indicate that the C activity in γ ahead of the growing α is larger than that ahead of θ, while the C activity of the bulk γ is larger than both for Alloy A and in between the two for Alloy B. To further investigate any possible bulk diffusion during the reaction, analyzing the local chemical composition of the product pearlite is a viable method. Of interest is the deviation of both the Mn and C content between the pearlite and the bulk γ, which is equal to the overall alloy composition for a large part of the reaction.

To determine the local composition of pearlite, both the reconstructed chemical composition as well as the phase fractions of the product phases are necessary and summarized for Alloys A and B in Tables 2 and 3, respectively. This allows for the actual composition of the pearlite to be calculated by:

$$\begin{pmatrix} X_C \\ X_{Mn} \end{pmatrix} = \begin{pmatrix} X_C^\alpha & X_C^\theta \\ X_{Mn}^\alpha & X_{Mn}^\theta \end{pmatrix} \begin{pmatrix} f_m^\alpha \\ f_m^\theta \end{pmatrix} \tag{3}$$

Here, X_Y represents the total molar fraction of the element Y within the pearlite in the region of interest, X_Y^Z is the molar fraction of Y in phase Z and f_m^Z is the molar fraction of phase Z. For Alloy A, the local composition of the pearlite is $X_C = 1.3$ at.% and $X_{Mn} = (3.0 \pm 0.2)$ at.% (vs. 2.9 at.% C and 2.8 at.% Mn in the alloy) and for Alloy B $X_C = 5.0$ at.% and $X_{Mn} = (7.2 \pm 0.6)$ at.% (vs. 2.9 at.% C and 6.9 at.% Mn in the alloy). For both cases, pearlite resembles the Mn content of the bulk γ (alloy composition), but not the C content. In the case of Alloy A, γ would become enriched in C during growth, while the C content in γ would have decreased in Alloy B. However, characteristic features in the microstructure suggesting such varying growth conditions were only observed in Alloy B. Here, depending on the orientation of the pearlite colonies to the surface, an increase in the lamellar spacing and a reduction in the θ fraction was observed. In Alloy A, no features corresponding to C enrichment of γ during growth were found. The reason for this is most likely the heterogeneity of the predominantly fibrous microstructure as the longitudinal axis of the fiber must be oriented parallel to the sample surface to clearly observe changes in spacing and phase fraction during growth.

These results were not consistently predicted by considering the C activity values of the SCA-LE method. The same holds true for the experimentally reconstructed SCA-LE data. Considering the deviation of the LE model from the present experimental data, SCA-LE in its current form does not seem suitable for accurate predictions in the investigated parameter space, ranging from 3 wt% Mn and 600 °C transformation temperature to 7 wt% and 540 °C, respectively. In addition to the underlying diffusion problem of simultaneous Mn and C partitioning, modelling pearlite formation in the two-phase-field specifically requires the consideration of two more aspects. The first one is the *apparent* steady-state character of the transformation. SCA-LE was developed with the goal of modelling a steady-state reaction [14]. This decision is

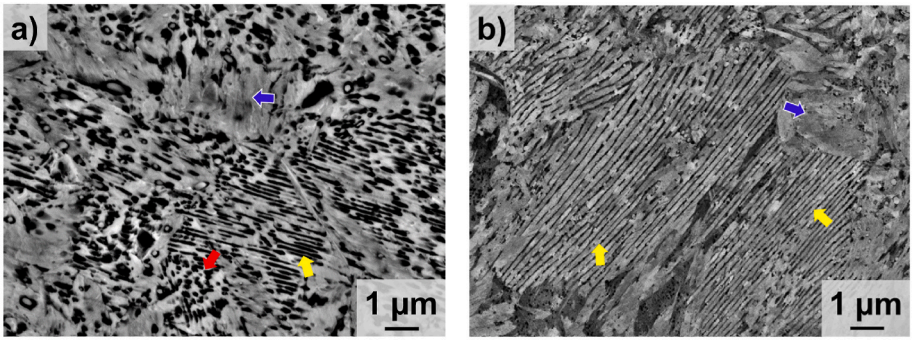

Fig. 8. a) and b) show micrographs of Alloys A and B using SEM-BSE (Nital etching) contrast after the STA treatment, respectively. No untransformed regions were observed for either alloy. Dark regions are γ, while medium gray regions are α'. Lamellar morphology is marked by yellow, the fibrous by red arrows. The blue arrows indicate regions without retained morphology.

based on the two steady-state features of the reaction, namely the near constant growth rate and interface spacing (for most of the reaction). However, while appearing as steady-state in this regard, the reaction most likely exhibits constant bulk C diffusion to or away from the reaction front for a large set of parameters. While SCA-LE addresses the constant volume fraction during growth by the design of the connecting line intersecting the alloy composition, the C activity difference between interface and bulk γ in most cases will violate steady-state requirements as a constant diffusion flux is enforced. Another aspect is the occurrence of different θ morphologies, which are a prominent feature in the present alloys but rarely addressed in literature. The difference in curvature of fibrous and lamellar θ at the reaction front might be too large to be neglected and might affect the LEs. In summary, a more precise LE model could be developed if adequate considerations of the (quasi-) steady-state conditions and the interface curvature at the reaction front are incorporated.

3.3. Short time austenitization

Apart from the theoretical models to describe the Fe–Mn–C pearlite reaction, the APT results clearly show a significant Mn partitioning between α and θ for both alloys. In order to validate if the respective Mn pattern is sufficient for the promising scheme introduced by Sun et al. [9], an STA treatment was performed. A successful STA treatment is considered an independent, statistically relevant proof of Mn partitioning, as the lamellar/fibrous α' + γ microstructure cannot be synthesized without it. The heat treatment was conducted at 770 °C for 150 s for both alloys and was concluded via oil quenching. Micrographs after the treatment can be seen in Fig. 8 a) and b) for Alloys A and B, respectively. For the given set of parameters, a complete transformation to γ was observed. The novel α' + γ microstructure can be easily distinguished from the initial pearlite as there is a contrast inversion in both SEM−SE and SEM-BSE contrast. While in pearlite the minority phase θ appears bright, the minority phase γ appears dark. Both alloys largely retained their morphology when compared to the initial pearlite, i.e. both still show fibrous (highlighted by red arrows in Fig. 8 a)) as well as lamellar (highlighted by yellow arrows in Fig. 8) domains. However, both alloys also show regions with no distinct morphology (highlighted by blue arrows in Fig. 8). After a region was transformed to γ, any additional hold time can be considered as a homogenization, where the Mn pattern gradually dissolves. The process is expected to be fastest in regions of small lamellar spacing, as well as weak Mn pattern. A significant local Mn homogenization may therefore be achieved already during the transformation to γ. For a given pearlitic sample, this can be partially or completely avoided by choosing the STA temperature sufficiently high to allow for a fast transformation. An STA temperature only slightly above A_3/A_{CM} (C- and Mn-dependent lower temperature limits, at which α/θ will be entirely transformed to γ) may result in a slow transformation, which allows already transformed regions to be homogenized before the microstructure is entirely austenitic. Substantially homogenized regions are unable to retain the aspired morphology, as the peak Mn content is insufficient to stabilize γ.

4. Conclusions

Two model alloys were subjected to a pearlite treatment fulfilling the Mn partitioning criterion only for α, but not for θ and therefore outside the established P-LE and NP-LE regimes. After the pearlite formation, an STA treatment was applied. With respect to the initial research questions R1 to R3, the following conclusions can be drawn.

R1: Even at low transformation temperatures and high Mn contents (540 °C and 6.9 at.%), a complete pearlite transformation is achieved with α and θ being the only constituting phases.

R2: Pearlite formation in the regime where the Mn partitioning condition is fulfilled only for α (and not for θ) still results in considerable Mn partitioning, indicating that partitioning occurs in a wider range of Mn and C contents as well as transformation temperatures than previously assessed in literature. Considering the similar composition and lattice constants of α in both alloys, it is likely that the low Mn equilibrium solubility of α is the decisive factor for the degree of partitioning between the two product phases. Thus, if the overall Mn content exceeds the solubility limit, noticeable Mn partitioning can be expected irrespective of predicted partitioning regimes. The detailed analysis of experimental APT data on two Fe–Mn–C alloys, one with a low and one with a high Mn content, suggests that the reaction cannot be described using the SCA-LE method under the above conditions. The reconstructed tie lines do not share a common C iso-activity in γ. Furthermore, the reaction does not follow conventional steady-state conditions, as already indicated in Ref. [14]. Despite a quasi-steady-state growth for most of the reaction, the pearlite inherits the overall alloy composition only with respect to the Mn content. The C content may vary during growth, enabling a significant deviation of the phase fractions within the quasi-steady-state regions compared to the predicted LE and GE values.

R3: The chemical Mn pattern in both alloys is sufficiently strong to achieve the anticipated α' + γ microstructure via STA from the initial pearlite. This provides independent proof of substantial Mn partitioning.

Prime novelty statement

We confirm that this manuscript has not been published previously by any of the authors and is not under consideration for publication in another journal.

Declaration of competing interest

The authors declare that they have no known competing financial interests or personal relationships that could have appeared to influence the work reported in this paper.

Acknowledgments

This work has been supported via personal grants by the Landesgraduiertenförderung (LGF) by the local state of Baden-Württemberg (Germany) and the GRAFÖG funding by the German Academic Exchange Service (DAAD). The authors gratefully acknowledge Karlsruhe Nano Micro Facility (KNMFi) for providing advanced instruments (proposal number: ha032044). The synchrotron XRD experiments (proposal no. 2024B1779) at SPring-8 (Super Photon ring-8 GeV) were conducted with the approval of the Japan Synchrotron Radiation Research Institute (JASRI). Furthermore, the authors thank Professors Christopher Hutchinson and Sebastian Weber for valuable discussions on the contents of this article.

Appendix A. Supplementary data

Supplementary data related to this article can be found online at https://doi.org/10.1016/j.jmrt.2025.11.194.

Data availability

The data presented in this study are available in Zenodo at https://doi.org/10.5281/zenodo.17136940 under CC BY-SA 4.0 license. The code including thermodynamic sample data is available here http://doi.org/10.35097/zxerv7gpadsje23a under the same license. Further information is available upon request with alexander.kauffmann@rub.de.

References

[1] Lavakumar A, et al. Role of surrounding phases on deformation-induced martensitic transformation of retained austenite in multi-phase TRIP steel. Mater Sci Eng, A 2023;874:145089.
[2] Hwang S, et al. Mesoscopic nature of serration behavior in high-Mn austenitic steel. Acta Mater 2021;205:116543.
[3] Tasan CC, et al. An overview of dual-phase steels: advances in microstructure-oriented processing and micromechanically guided design. Annu Rev Mater Res 2015;45:391–431.
[4] Song R, et al. Overview of processing, microstructure and mechanical properties of ultrafine grained bcc steels. Mater Sci Eng, A 2006;441(1):1–17.
[5] Bhadeshia HKDH. Nanostructured bainite. Proc R Soc A 2009;466(2113):3–18.
[6] Tsuji N, et al. Ultra-fine grained bulk steel produced by accumulative roll-bonding (ARB) process. Scr Mater 1999;40(7):795–800.
[7] Yao MJ, et al. Strengthening and strain hardening mechanisms in a precipitation-hardened high-Mn lightweight steel. Acta Mater 2017;140:258–73.
[8] Raabe D, et al. Current challenges and opportunities in microstructure-related properties of advanced high-strength steels. Metall Mater Trans A 2020;51(11):5517–86.
[9] Sun WW, et al. Advanced high strength steel (AHSS) development through chemical patterning of austenite. Scr Mater 2018;146(5):60–3.
[10] Li S, et al. Study of partition to non-partition transition of austenite growth along pearlite lamellae in near-eutectoid Fe-C-Mn alloy. Acta Mater 2019;177:198–208.
[11] An XL, et al. The role of retained austenite on the stress-strain behaviour of chemically patterned steels. Mater Sci Eng, A 2022;831:142286.
[12] Yang D, et al. Mn heterogeneity and ductility improvement realized by slow heating Mn-Partitioned pearlite. Met Mater Int 2024;30(2):393–402.
[13] Yang D, et al. The abnormal carbon redistribution in lath martensite during tempering in Mn-patterned steels. Mater Char 2024;210:113841.
[14] Hutchinson CR, et al. The growth of partitioned pearlite in Fe–C–Mn steels. Acta Mater 2004;52(12):3565–85.
[15] Hillert M. Phase equilibria, phase diagrams and phase transformations: their thermodynamic basis. In: Phase equilibria, phase diagrams and phase transformations: their thermodynamic basis. Cambridge: Cambridge University Press; 2007. p. 358–66.
[16] Kirkaldy JS. Diffusion in multicomponent metallic systems: ii. solutions for two-phase systems with applications to transformations in steel. Can J Phys 1958;36(7):907–16.
[17] Coates DE. Diffusional growth limitation and hardenability. Metall Trans A 1973;4(10):2313–25.
[18] Benz R, et al. Thermodynamics of the solid phases in the system Fe−Mn−C. Metall Trans A 1973;4(8):1975–86.
[19] Shen YZ, et al. M5C2 carbides in a high-chromium ferritic/martensitic steel. Metall Mater Trans A 2014;45(7):2950–62.
[20] Cheng W-C, et al. On the eutectoid reaction in a Quaternary Fe-C-Mn-Al alloy: Austenite → ferrite + kappa-carbide + M23C6 carbide. Metall Mater Trans A 2014;45(3):1199–216.
[21] Eckel JF, Krivobok VN. Alloys of iron, manganese and carbon-part VIII. Trans Am Soc St Tr 1933;21:846–64.
[22] Gensamer M. Alloys of iron and manganese-part XII. Trans Am Soc St Tr 1933;21:1028–34.
[23] Hillert M, Waldenström M. A thermodynamic analysis of the Fe-Mn-C system. Metall Trans A 1977;8(1):5–13.
[24] Stefanescu D, Katz S. Thermodynamic properties of iron-base alloys. In: Viswanathan S, et al., editors. Casting. Ohio: ASM International; 2008. p. 41–55.
[25] Bain EC, et al. The equilibrium diagram of iron-manganese-carbon alloys of commercial purity. Tran Am Inst Min Metall Eng 1932;100:228–56.
[26] Tofaute W, Linden K. Die Umwandlung im festen Zustande bei Manganstählen mit Gehalten bis 1,2% C und 17% Mn. Arch für das Eisenhuttenwes 1937;10(11):515–24.
[27] Vogel R, Döring W. Das System Eisen-Zementit-Mangankarbid-Mangan. Arch für das Eisenhuttenwes 1935;9(5):247–52.
[28] Walters FM, Wells C. Alloys of iron and manganese-part XIII. Trans ASM 1935;23(3):727–50.
[29] Walters FM, Wells C. Alloys of iron, manganese and carbon-part XIV. Trans ASM 1935;23(3):751–60.
[30] Muench M, Kauffmann A. Matlab code to 'Assessment of the Compositional Requirements to form Fe-Mn-C Austenite-Martensite Composites'. Karlsruhe Institute of Technology; 2025.
[31] Gault B, et al. Atom probe tomography. Nat Rev Methods Primers 2021;1(1):1–30.
[32] Schwarz TM, et al. In situ metallic coating of atom probe specimen for enhanced yield, performance, and increased field-of-view. Microsc Microanal 2024;30(6):1109–23.
[33] Muench M, Kauffmann A. Completion of Pearlite Transformation in Fe-Mn-C Alloys with 3 and 7 wt.% Mn. Zenodo; 2025.
[34] Zhou DS, Shiflet GJ. Ferrite: cementite crystallography in pearlite. Metall Trans A 1992;23(4):1259–69.
[35] Peng Z, et al. Unraveling the metastability of Cn2+ (n = 2–4) clusters. J Phys Chem Lett 2019;10(3):581–8.
[36] Takahashi J, et al. Study on quantitative analysis of carbon and nitrogen in stoichiometric θ-Fe3C and γ′-Fe4N by atom probe tomography. Microsc Microanal 2020;26(2):185–93.
[37] Bhadeshia HKDH. Some difficulties in the theory of diffusion-controlled growth in substitutionally alloyed steels. Curr Opin Solid State Mater Sci 2016;20(6):396–400.
[38] Cahn JW, Hilliard JE. Free energy of a nonuniform system. I. Interfacial free energy. J Chem Phys 1958;28(2):258–67.
[39] Cahn JW, Hilliard JE. Free energy of a nonuniform system. III. Nucleation in a two-component incompressible fluid. J Chem Phys 1959;31(3):688–99.
[40] Hillert M. A solid-solution model for inhomogeneous systems. Acta Metall 1961;9(6):525–35.
[41] Cahn JW. On spinodal decomposition. Acta Metall 1961;9(9):795–801.
[42] Gouné M, et al. Overview of the current issues in austenite to ferrite transformation and the role of migrating interfaces therein for low alloyed steels. Mater Sci Eng R Rep 2015;92:1–38.
[43] Ågren J, et al., editors. Thermodynamics and Phase Transformations: The selected works of Mats Hillert. Les Ulis: EDP Sciences; 2021. p. 7.